Physics – Uspekhi **69** (3) 205 – 220 (2026)

REVIEWS OF TOPICAL PROBLEMS

PACS numbers: 52.30.Cv, 52.35.Py, 52.58 Lq

Simulations of Z-pinches

S.F. Garanin, V.Yu. Dolinskii

DOI: https://doi.org/10.3367/UFNe.2025.08.039998

Contents

Abstract. Studies of the development of a 'sausage' instability of Z-pinch in the MHD-approximation and the account for the development of two-dimensional turbulence have shown that turbulence development prevents the formation of the neck with an infinitely decreasing radius. Under the neck compression in this approximation there is also no generation of high voltages near the axis that could contribute to the formation of ion beams and neutrons generation due to the beam-target mechanism. Thus, to describe neutron generation in the beam–target mechanism, it is necessary to take into account the kinetic processes of high voltage generation in plasma. 2D MHD-computations with the account for kinetic processes in the phenomenological form of anomalous resistivity make it possible to achieve for a number of plasma focus configurations and gas puff Z-pinch an agreement with experimental data on current, voltage and neutron measurements. 2D kinetic computations of the plasma focus carried out for the final phase of pinch formation agree with experimental data on the neutron yield and distribution of ions in the resulting beams and confirm that the anomalous plasma resistivity may be due to lower hybrid drift instability, which was assumed in phenomenological MHD-computations that describe neutron generation in Z-pinch and plasma focus.

Keywords: MHD-simulations, plasma dynamics, 'sausage' instability, Z-pinch, plasma focus

1. Introduction

Z-pinches are traditionally defined as dynamic systems in which the magnetic field has only an azimuthal component, and all quantities are primarily axisymmetric and depend on two cylindrical coordinates, r and z. Z-pinches include plasma focus discharges, axisymmetric systems with pulsed gas injection, wire discharges, and so-called Z-pinch-liner systems with cylindrical implosion of relatively thin liner shells, including even not entirely axisymmetric multi-wire liners.

Plasma focus discharges are a special case of the Z-pinch [1–4], distinguished by the geometry of the plasma chamber, which allows for the separation of the current plasma sheath motion stage within the chamber volume from the pinching stage, based on characteristic times. Consequently, slower current sources can be used to generate the pinches. The earliest experiments with Z-pinches were conducted in the 1950s [5–7], when researchers aimed to heat the plasma and ignite thermonuclear reactions, assuming a Maxwellian ion distribution in each volume element. Under this assumption, ion collisions would lead to thermonuclear fusion reactions and neutron generation (the thermonuclear mechanism). However, even in early Z-pinch experiments, it was found that the resulting neutrons were not thermonuclear, but were produced by collisions of ions accelerated to energies far exceeding thermal values with the pinch plasma ions. This neutron generation mechanism is known as the beam–target mechanism.

In the mid-1950s, T.I. Filippova and N.V. Filippov [8], and somewhat later J.W. Mather [9], independently proposed, investigated, and published two modifications of cylindrical coaxial gas-discharge chambers with metal walls. In these chambers, during the initial stage of a high-voltage discharge in rarefied deuterium, a current plasma sheath (CPS) forms around the insulator and is accelerated by the magnetic field of the discharge current. As the sheath converges toward the chamber axis, partial sweeping and compression of the neutral gas occurs. As a result, when the CPS collapses in the paraxial region, a dense plasma focus (DPF) with high energy density is formed. In the early 1960s, at the VNIIEF, under the direction of N.G. Makeev, research began on a new original spherical gas-discharge chambers with DPF. The chambers were called SFK [10, 11]. The anode and cathode in the chamber are spherical, forming a compact, extended gas-discharge gap through which the CPS propagates, smoothly changing direction by 180° during the discharge.

S.F. Garanin*, **V.Yu. Dolinskii**
Russian Federal Nuclear Center–All-Russian Research Institute of Experimental Physics,
prosp. Mira 37, 607188 Sarov, Nizhny Novgorod region, Russian Federation
E-mail: * sfgaranin@vniief.ru

Received 10 June 2025, revised 7 August 2025
Uspekhi Fizicheskikh Nauk **196** (3) 221 – 237 (2026)
Translated by I.A. Ulitkin

Achieving high neutron yields in experiments with 100 ns current generators played an important role in studying neutron generation in the Z-pinch. For example, at the Angara-5-1 facility [12], significant neutron yields of up to 8×10^{11} DD neutrons per pulse were obtained at currents of 2–2.5 MA, and similar studies were performed at the S-300 facility [13]. The effect of the size and duration of a plasma-focus pinch [14], as well as the current amplitude [15], influences neutron generation, and elucidating this relationship may also aid in research into the neutron generation mechanism. It is also necessary to mention the experimental studies at the PF-1000 facility (see, for example, [16]), which also investigated the neutron generation mechanism and, in particular, examined the effect of anomalous resistivity on the current disruption in the pinch. Important information about the neutron generation mechanism can be obtained from experimental data on the neutron yield anisotropy [17]. In recent years, active studies of the neutron generation mechanisms in Z-pinches and the plasma focus have continued. In particular, works [18–20] report the detection of ions accelerated to energies of tens of MeV in Z-pinches and discuss possible mechanisms for the generation of such energetic ions and their contribution to neutron production.

In the early 2000s, experiments at the Z facility [21–23] demonstrated neutron yields of 4×10^{13} DD neutrons at a current level of 18 MA, with results indicating a predominantly thermonuclear mechanism of neutron generation. In addition to a noticeable shortening of the current pulse, an essential difference of the experiments at the Angara-5-1 and Z facilities from the classical Z-pinch is the use of pulsed gas puffing into the discharge gap, which creates a nonuniform deuterium density distribution and concentrates its bulk near the axis where the plasma sheath is focused. It should be noted that gas puffing has also been used in plasma focus devices [24–26], where its use as the primary or additional source of deuterium in combination with stationary gas puffing allowed the neutron yield to be increased, compared to operation in the stationary gas puffing.

Despite the long history of Z-pinch and plasma-focus research, there is still no complete understanding of the pinch dynamics and a unified model of neutron generation that would explain all experimental data and allow for confident prediction of experimental results. An important stage of this research was the study of the development of sausage instability. References to papers devoted to this issue can be found in reviews [1, 2], and further studies are presented in [27–30]. The solutions describing magnetohydrodynamic (MHD) behavior were unstable, but the authors (usually tacitly) assumed that MHD instability would not eliminate the general relationships obtained using these unstable solutions. A vigorous discussion of the neutron generation mechanisms was presented in review articles published in *Sov. J. Plasma Physics* in the late 1980s and early 1990s [31–33]. The Lee model [34, 35] has been widely used to model the CPS dynamics and neutron yield in plasma focus devices; however, it remains phenomenological and well adapted only to Mather-type plasma focuses [9].

In recent decades, significant progress has been made in the computational and theoretical simulation of Z-pinches and plasma focus systems, as well as in understanding the phenomena occurring in plasma dynamics during pinching and the processes leading to neutron generation in Z-pinches. This was facilitated by significantly increased computing capabilities, which now make it possible to simulate the turbulent development of instabilities (including the sausage instability, crucial for describing the Z-pinch necking) and even directly simulate electron-ion kinetics during pinching. Studies of the Z-pinch necking in the axisymmetric MHD approximation and taking into account the development of two-dimensional turbulence have shown that turbulence suppresses the formation of a neck with an infinitely decreasing radius and plasma outflow from the compression region. During neck compression in this approximation, high voltages are not generated near the axis, which could facilitate the formation of ion beams and neutron generation due to the beam–target mechanism. In the calculations, an MHD equilibrium state is rapidly established near the margin of the interchange instability. Thus, to describe neutron generation via the beam–target mechanism, it is necessary to take into account the kinetic processes of high-voltage generation in the plasma. Two-dimensional MHD calculations taking into account kinetic processes in the phenomenological form of anomalous resistivity make it possible to achieve agreement with experimental data on current, voltage, and neutron measurements for a number of plasma focus configurations, as well as agreement with the neutron yield for the fast Z-pinch, in which the beam–target mechanism provides only a portion of the neutron yield.

Incorporating a kinetic description of the motion of charged particles (e.g., in the particle-in-cell approximation) in the CPS focusing region and coupling this description with the MHD approach for the rest of the plasma focus region [36–38] appears to be a promising approach, but is very labor-intensive and computationally expensive. Apparently, this approach has not yet been developed to a level where it can be considered fully kinetic. In recent years, active studies of the mechanisms of neutron generation in Z-pinches and plasma focus have continued.

In this paper, we discuss modern approaches for computational simulation of Z-pinches, including a description of their dynamics and neutron generation.

2. Plasma dynamics during the development of Z-pinch necking

The general trend of plasma dynamics in the plasma focus and other Z-pinch configurations during the final stage is plasma compression toward the axis. At this final stage, the pinch is subject to MHD instabilities, the most significant of which is the axisymmetric sausage instability, leading to the formation of so-called necks, i.e., paraxial constrictions of the plasma column. The energy density increases in these necks, and it is generally assumed that neutrons and hard radiation are generated within them.

As the sausage instability develops, the equilibrium distribution of quantities in the Z-pinch is determined by the Bennett condition [39], and axial symmetry (mode $m = 0$) is preserved within the sausage instability itself. Then, the magnetic field outside the pinch depends on the radius as $B \sim 1/r$, and, consequently, the magnetic pressure on the pinch plasma will be proportional to $p_B \sim 1/r^2$. In this case, the plasma regions that have contracted along the radius under increased magnetic pressure will undergo further compression even more sharply, leading to the growth of perturbations.

The linear stage of Z-pinch instability development was first studied in papers [40–42]. The instability growth rates λ for the azimuthally symmetric mode $m = 0$ for a skinned pinch (whose radius R exceeds the skin depth) are equal to:

• for short-wavelength perturbations ($kR \gg 1$), the sausage instability reduces [30] to Rayleigh–Taylor (RT) instability and has a growth rate,

$$\lambda = \sqrt{gk}\,, \tag{1}$$

where

$$g = \frac{B^2}{4\pi\rho R} = \frac{c_A^2}{R} \tag{2}$$

is the effective gravitational acceleration, $c_A = B/\sqrt{4\pi\rho}$, B is the magnetic field at the pinch radius, and ρ is the density of the pinch material;

• for long-wavelength perturbations ($kR \ll 1$),

$$\lambda = \sqrt{\frac{\gamma}{2(\gamma-1)}}\, c_A k\,, \tag{3}$$

where γ is the adiabatic index.

If the pinch is not skinned and all quantities in it are distributed over the radius, then for short wavelengths ($kR \gg 1$), the sausage instability growth rate can be determined for each value of the radius. These growth rates should, at $kr \gg 1$, tend to a constant value depending on the gradients of the logarithm of $\Phi = p^{1/\gamma} r/B$ [30]

$$\lambda^2 = -\frac{2c_A^2}{r^2}\frac{\partial \ln \Phi}{\partial \ln r}\,, \tag{4}$$

where the pressure p and magnetic field B are taken for the current radius r.

Thus, linear theory predicts that the sausage instability can develop increasingly rapidly as the pinch radius decreases. Therefore, historically, when considering Z-pinches, it was generally assumed that, at the final stage of instability development, extremely high magnetic fields and energy densities could be achieved in the neck region. Studying the nonlinear development of sausage instability is a complex problem, since the growth rates increase with decreasing spatial scales. Various methods have been used to study this issue (see, for example, reviews [1, 2] and references therein), including model problems, particular ideal solutions (ignoring the growth of the entire spectrum of perturbations), analytical solutions [27], and self-similar [29, 30] solutions. Various hypotheses have been put forward that, at the final stage of compression, the neck dynamics will follow self-similar behavior. For example, assuming adiabatic compression and that the neck length l is proportional to its radius R and the plasma outflow time from the neck region is $t \sim l/v_T \sim R/v_T$ (v_T is the speed of sound in the neck), we obtain [2] the time dependences of the radius, plasma density ρ, and plasma temperature T (we assume t to be negative, $t \to 0$, so that the radius vanishes at $t = 0$)

$$R \sim (-t)^{\gamma/(2\gamma-1)}\,, \quad \rho \sim (-t)^{-2/(2\gamma-1)}\,,$$
$$T \sim (-t)^{-2(\gamma-1)/(2\gamma-1)}\,. \tag{5}$$

However, assuming adiabatic compression with a fixed neck length (analytical solutions [27] and numerical calculations [29, 43] seemed to support such a scenario), the characteristic quantities will change as follows:

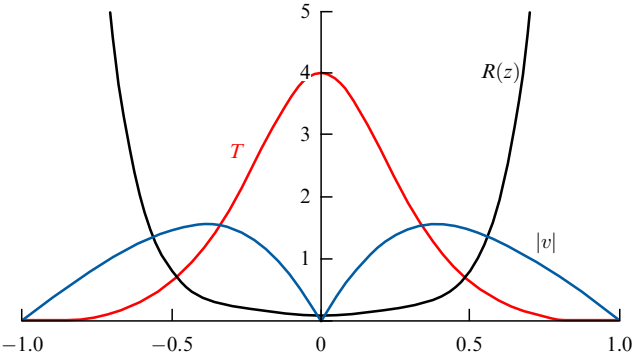

Figure 1. The shape of the neck at the self-similar stage — the $R(z)$ curve and the distribution of temperature T and longitudinal velocity $|v|$ along the neck length [29, 30].

$$R \sim (-t)^{\gamma/(\gamma-1)}\,, \quad \rho \sim (-t)^{-2/(\gamma-1)}\,,$$
$$T \sim (-t)^{-2}\,. \tag{6}$$

and the corresponding self-similar solution [29, 30] is shown in Fig. 1.

Moreover, for any of these dependences (5) and (6), as $t \to 0$, the radius R tends to zero, the magnetic field at this radius tends to infinity $B \sim 1/R$ (the current determining the magnetic field 'reaches' this radius), and, consequently, high energy densities $B^2 \sim 1/R^2$, $p \sim 1/R^2$ should be realized. The difference between scenarios (5) and (6) is only in the time it takes for these conditions to be realized and in what volumes. When considering these solutions, the authors generally understood that these solutions are unstable, but still assumed that instabilities will not fundamentally change the general nature of self-similarity, and that instabilities will develop against the background of these solutions, and the solutions themselves will help explain interesting phenomena in Z-pinches, including the origin of neutron generation and penetrating radiation.

Garanin and Chernyshev [29] numerically calculated the development of a skinned neck under ideal assumptions (ignoring magnetic diffusion and in the complete absence of small-scale perturbations). They found that in this case, regime (6) is realized, in which the neck length l does not decrease with decreasing radius. However, achieving strong compressions in the numerical calculation turned out to be impossible due to development of instabilities. The maximum radial compression obtained in these calculations was 5.2 times.

High energy densities, which could potentially be realized in Z-pinch necks, gave hope for thermonuclear ignition (see, for example, [33, 44], where for regime (5), it was considered possible to obtain a radial compression of 10^4, achieve the Lawson criterion, and then thermonuclear detonation) or, at least, to obtain a high neutron yield.

In addition, the beam–target mechanism of neutron generation could result from high voltages that develop when a significant magnetic flux is lost near the axis in short times corresponding to the maximum compression of the neck. The active studies of neutron generation mechanisms in Z-pinches and plasma focus [18–20], where ions accelerated to

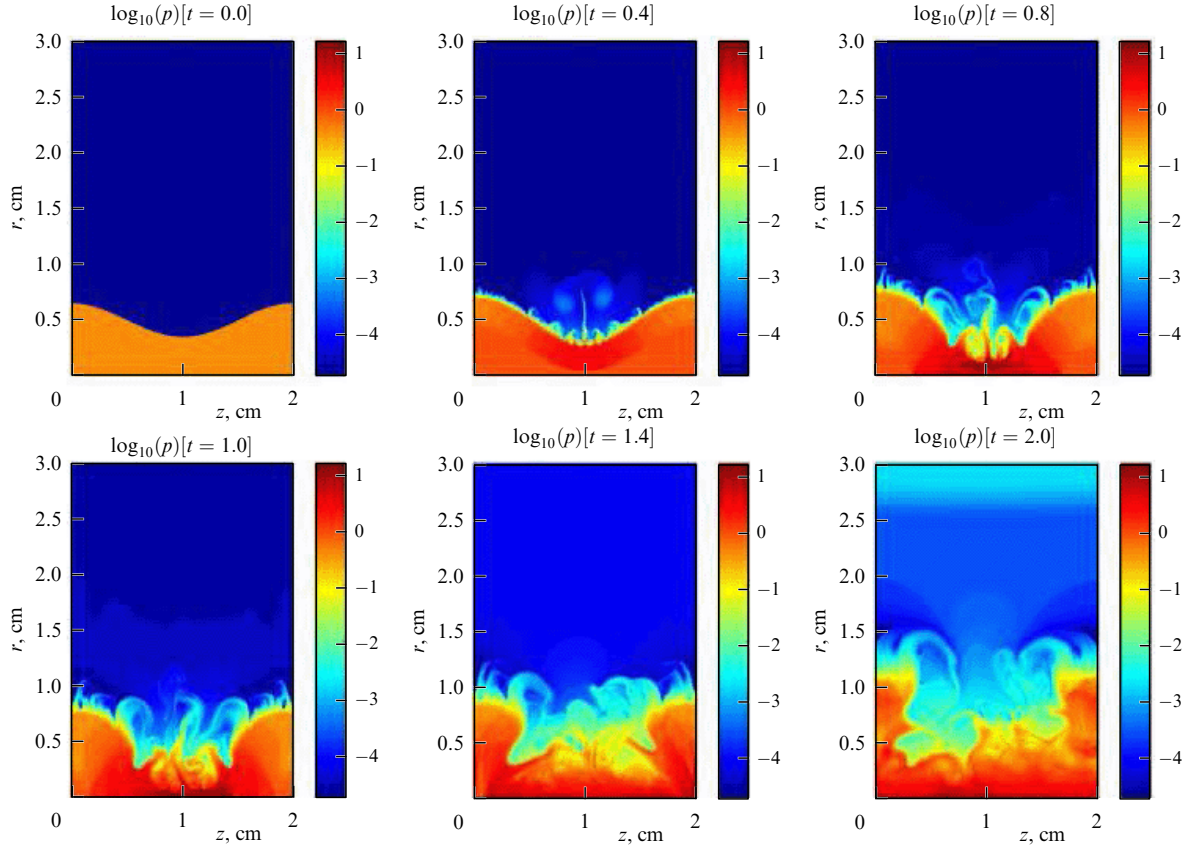

Figure 2. 2D distributions of pressure p for $a = 0.3$ [48].

tens of MeV are formed in the Z-pinch, have been ongoing in recent years. Among the possible mechanisms for this generation, both the development and rupture of the neck are discussed. It should be noted that in these studies, as well as in the studies cited in [45], which also consider the formation and development of necks, the energies of ions recorded at various facilities exceed by tens (and even hundred) times the energies that can be provided by the initial voltages on the current generators used in the experiments.

An approach for calculating the neutron yield in a plasma focus was proposed in [46]. This approach, in addition to the MHD calculation, takes into account the motion of ion beams accelerated by the voltage induced by the anomalous resistivity in the focusing region. The collision of accelerated ions with the dense plasma in the focusing region leads to neutron generation, and it was shown in [46, 47] that this approach provides a good description of experimental neutron generation results for a number of plasma-focus geometries. This approach can also be based on the neck development mechanism, and the neutron yield here may also depend on whether current penetration to a small radius and the escape of significant magnetic flux to the axis are possible within a short time.

Thus, a common question for all these problems and phenomena is whether neck development can drive the current to small radii and form a region with high energy density, or create conditions for the generation of high voltages near the axis. This issue was investigated using axisymmetric MHD calculations [48], assuming that magnetic diffusion and thermal conductivity are unimportant, but taking into account, to the greatest possible extent, the entire spectrum of small perturbations that could influence the neck development.

The calculations considered the evolution of a cylindrical plasma column with a sinusoidal perturbation of the boundary and small random density perturbations. To enable self-similar recalculation of the problem for any systems (currents, densities, etc.), the pinch current was assumed constant.

The calculations showed that, due to the development of turbulence, the formation of a small-radius neck and plasma outflow from the compression region do not occur. Instead, mixing and closure of the compression region by plasma jets occurs (Fig. 2). As a result, the pressures, densities, and magnetic fields in the compression region do not increase indefinitely as the compression proceeds, but stabilize. For the relative initial perturbation amplitude of $a = 0.3$ (the absolute amplitude of the initial perturbation is aR_0, R_0 is the initial radius of the pinch), the pressure increased by a factor of 65, and the magnetic field by a factor of 4.

The calculations showed that the development of sausage-like perturbations stabilizes over time. The plasma then reaches an equilibrium state at the margin of Kadomtsev instability

$$\frac{\mathrm{d}\ln p}{\mathrm{d}\ln r} \geqslant -\frac{4\gamma}{2+\beta\gamma} \qquad (7)$$

($\beta \equiv p/(B^2/8\pi)$) [49]. Of course, this equilibrium is dynamic, and turbulent dynamic pulsations occur against its background. Figure 3 compares the pressure profiles obtained

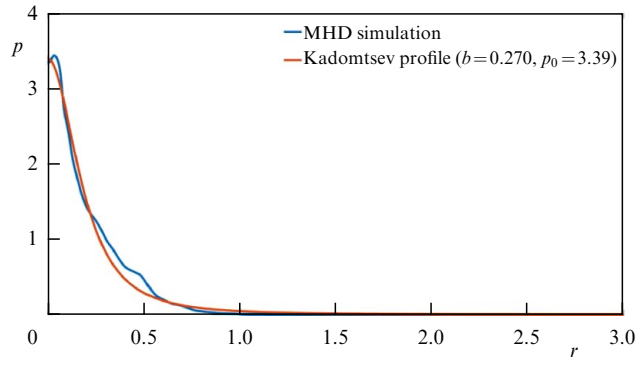

Figure 3. Comparison of the MHD simulation results and Kadomtsev profiles (at the margin of the interchange instability) for pressure at the time corresponding to the maximum pinch compression [48].

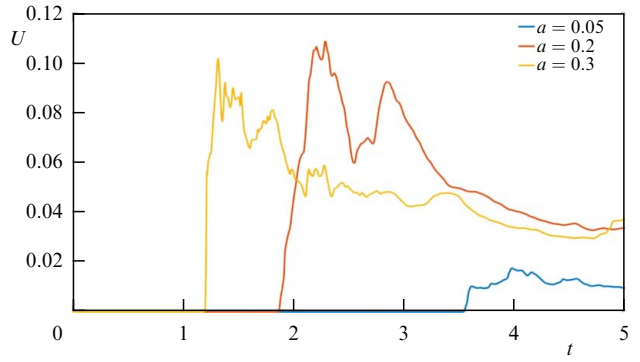

Figure 4. On-axis voltages for simulations with $a = 0.05$, 0.2, and 0.3 [48].

from the MHD calculation with $a = 0.05$ at $t = 2.4$ and the Kadomtsev profiles (see Appendix), the parameters of which were selected based on the best agreement with the profiles from the MHD calculation. The average radial pressure profiles in the MHD calculations were obtained by averaging the 2D distributions over z.

When the neck is compressed, no high voltages are generated near the axis (Fig. 4), which could facilitate the formation of ion beams and neutron generation due to the beam–target mechanism. Thus, in calculations with $a = 0.3$, the voltages are approximately equal to $0.1U$, where U is the characteristic voltage determined by the current, pinch inductance, and pinching time.

Here, we can also hypothesize what will happen in three-dimensional calculations when taking into account generation due to the MHD instability of the poloidal $r-z$ fields. In this case, assuming that the emerging poloidal fields remain relatively small (compared to azimuthal ones), the development of instability can lead, similarly to the development of sausage instability (see Fig. 3), to the formation of an equilibrium state of the Z-pinch at the instability margin, including sausage (7) and helical ($m = 1$)

$$\frac{\mathrm{d}\ln p}{\mathrm{d}\ln r} \geqslant -\frac{1}{\beta}\,, \tag{8}$$

instabilities [the dependences of the main quantities on the radius at the instability margin, when equalities in conditions (7) and (8) are satisfied, are presented in the Appendix]. Of course, as for sausage instability, the equilibrium here will be dynamic; i.e., on average, and against the background of this equilibrium, pulsations will occur, leading to energy dissipation and magnetic flux losses.

Work [48] changes the philosophy regarding the feasibility of self-similar solutions for unstable Z-pinch problems. It was previously assumed that, although such solutions are unstable, this instability should not destroy them completely, preserving their overall scale and fundamental trends and manifesting itself as a relatively small ripple against the background of a somewhat distorted self-similar solution. However, it was shown that nothing remains of the self-similar solution, and so the previously obtained self-similar solutions have no physical meaning (at least for the large compressions they were intended to achieve).

As for thermonuclear applications, if we consider a current of $I = 10$ MA and a characteristic time of 10^{-7} s for the neck problem under consideration, the resulting values of temperature and ρr are far from those required for igniting a thermonuclear reaction. Even increasing the current to 100 MA may not lead to ignition in this scenario.

3. Z-pinch simulation including neutron generation

Thus, since MHD neck development does not lead to either significant energy density concentration or strong on-axis electric fields, plasma microturbulence must be invoked to explain the generation of high-energy ion and neutron beams using numerical simulation. Currently, there exist two main approaches: a semi-phenomenological approach, which incorporates anomalous plasma resistivity caused by plasma instabilities, leading to ion beam formation, into MHD simulations; and a fully kinetic approach, which explicitly accounts for the kinetics of ions and electrons. Let us consider these approaches.

3.1 MHD simulation with ion beam formation via anomalous resistivity

The approach to describing processes in Z-pinches [46, 47], based on two-dimensional MHD calculations, takes into account the motion of ion beams accelerated by the electric fields generated due to anomalous resistitvity in the focusing region. Plasma motion in the calculations was described using two-temperature magnetohydrodynamics equations in cylindrical coordinates, including magnetic field diffusion, radiation, and plasma thermal conduction.

Classical Spitzer formulas are used to calculate plasma conductivity, taking into account electron scattering by neutrals:

$$\frac{1}{\sigma} = \frac{1}{\sigma_{\mathrm{ei}}} + \frac{1}{\sigma_{\mathrm{en}}}\,, \tag{9}$$

where

$$\sigma_{\mathrm{ei}} = 5.44 \times 10^{11}\,\frac{T_{\mathrm{e}}^{3/2}}{L_{\mathrm{e}}}\,k\,,$$

$$\sigma_{\mathrm{en}} = \frac{\alpha}{1-\alpha}\,\max\left(3.7 \times 10^{8}, \sigma_{\mathrm{ei}}\right),$$

L_{e} is the Coulomb logarithm for electrons, α is the degree of ionization and k is the conductivity magnetization coefficient [50, 51].

When describing the conductivity, anomalous resistivity due to the development of plasma instabilities was also taken

into account. Accounting for anomalous resistivity is a key factor in neutron generation via the beam–target mechanism in this approach, since it leads to the formation of electric fields near the pinch axis capable of accelerating ions to high energies. These ions subsequently collide with the pinch plasma, producing neutrons. Various plasma conductivity models based on the development of lower-hybrid drift instability can yield different anomalous resistivity values [52–55]. In paper [47], use was made of the following anomalous resistivity model [52]:

$$\kappa_{\text{anom}} = \begin{cases} \dfrac{0.015\beta_{\text{ucs}}^2}{B\sqrt{A}}\,, & \beta_{\text{ucs}}^2 \leqslant 3 \\ \dfrac{0.045}{B\sqrt{A}}\,, & \beta_{\text{ucs}}^2 > 3 \end{cases}$$

$$\sigma_{\text{anom}} = \frac{c^2}{4\pi\kappa_{\text{anom}}}\,, \quad \sigma = \min\left(\sigma, \sigma_{\text{anom}}\right), \tag{10}$$

where β_{ucs} is the ratio of the current velocity to the ion thermal velocity, B is the magnetic field measured in Oe $\times 10^7$, A is the ion atomic mass (g mol^{-1}), and $c = 3000$ is the speed of light measured in cm s^{-1} $\times 10^7$. This model provides good agreement with experimental data on the neutron yield, as well as shape and position of the neutron source.

In our calculations, we only considered the electrical resistivity of the plasma and electron and ion thermal conductivities of the classical kinetic coefficients, while in the kinetic coefficients we took into account the magnetization of electrons and ions. Some two-fluid effects of magnetized plasma were neglected in our calculations, although they may be important for calculating magnetothermal processes in magnetoinertial confinement [30] and for describing the dynamics of low-density Z-pinches. These effects include transport phenomena represented by the Hall, Ettingshausen, Nernst, and Righi–Leduc effects in the generalized Ohm's law and in the expression for the heat flux, and described using classical kinetic coefficients [49, 50]. In Z-pinch simulations, their role may be more important in the neck region, where the linear plasma density decreases. In the neck region, where $\beta \sim 1$ and the plasma is magnetized, the ion linear number [56] $\Pi_{\text{i}} \equiv Ne^2/m_{\text{i}}c^2$, where $N = \int_0^\infty n2\pi r\,\mathrm{d}r$, can be used as a criterion for the degree of 'hydrodynamicity' of the plasma description. At large Π_{i}, the role of these effects should be minor. In our case, during the neck formation stage, Π_{i} is large enough for these effects to be neglected. At the neck decay stage, the ion linear number is $\Pi_{\text{i}} \sim 1$. However, at this time, anomalous resistivity is present, the effective turbulent collision frequencies greatly exceed the classical Coulomb ones, and classical kinetic coefficients are inapplicable. Therefore, the description of the neck plasma in this regime is largely phenomenological.

In this approach, the mechanism for the formation of accelerated ions in the plasma is governed by the presence of a sufficiently strong electric field, which is formed during the MHD description of a plasma with anomalous resistivity. Its action then turns out to be broadly similar to the phenomenon of electron runaway [51].

During runaway, electrons with sufficiently high energies are accelerated indefinitely in an electric field, since the Coulomb drag force acting on an energetic electron from ions and other electrons decreases as its velocity increases. However, for ions, in the case of classical (Spitzer) plasma resistivity, the force from the electron 'wind,' i.e., the force of electron resistivity, does not decrease with increasing ion velocity and there is no reason for ion escape [46].

The situation may change if the electric fields in the plasma are caused by anomalous resistivity. In this case, since the ions interact with the electrons through plasma-induced oscillations, the frictional force due to the electron 'wind' may depend significantly on the ion velocity. In many cases, the oscillations, induced in plasma interact strongly with the bulk of the ions and weakly with the energetic ions. (In particular, this may be true for the anomalous resistivity [52] associated with the lower-hybrid drift instability [53], for which the phase velocities of oscillations are on the order of $v_{\text{Ti}} = \sqrt{T_{\text{i}}/m_{\text{i}}}$, and therefore these oscillations can interact strongly with the bulk of the ions and weakly with the energetic ions.) Then, it can be assumed that the energetic ions are affected only by the electric field and the Coulomb drag forces [57] from the remaining ions and electrons, and the process of their acceleration under the influence of only these forces can be considered.

The total drag force F, resulting from the drag forces exerted by ions and electrons, depends on the ion velocity v_{i} and can be written as

$$F(x) = \frac{4\pi\lambda_{\text{i}}e^4 n}{T_{\text{i}}}\,\varphi(x)\,,$$

where the dimensionless force φ depends on the dimensionless velocity of the probe ion $x \equiv [m_{\text{i}}v_{\text{i}}^2/2T_{\text{i}}]^{1/2}$, the electron-to-ion mass ratio, and the ratio of their temperatures. For a deuterium plasma and equal electron and ion temperatures, the dependence $F(x)$ is shown in Fig. 5 [46].

The force $F(x)$ as a function of velocity has a minimum. If the force exerted by the electric field on the ion eE begins to equal or exceed this minimum value, then in the velocity range where $F(v_{\text{i}}) \sim eE$, one can expect the ion distribution function to be enriched in energetic ions. These energetic ions can readily undergo thermonuclear reactions and increase the neutron yield.

The neutron yield due to the acceleration mechanism was calculated as:

$$\left.\frac{\mathrm{d}Y}{\mathrm{d}t}\right|_{AC} = \int \alpha_{\text{i}}\frac{j_z}{e}\,n\sigma(\varepsilon_{\text{i}})2\pi r\,\mathrm{d}r\,\mathrm{d}z\,,$$

where n is the density of reacting plasma nuclei; α_{i} is the fraction of the current carried by ions; j_z is the axial current density component; and $\sigma(\varepsilon_{\text{i}})$ is the cross section of the DD or DT reaction, depending on the energy of the accelerated ion ε_{i}.

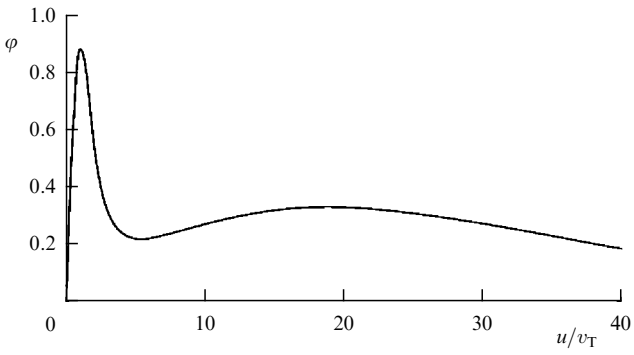

Figure 5. Dependence of the plasma drag force on the dimensionless deuteron velocity u/v_{T} [46].

To estimate this neutron yield, it was assumed that near the axis, within several Larmor radii of the accelerated ions, a fraction of the ions is accelerated along the axis in the electric field, simultaneously experiencing a drag force F. This force F was calculated using the formulas from [46, 57]. It was assumed that the accelerated ions carry $\alpha_i \sim 15\%$ of the maximum (up to the current value z) current density j_z in the near-axial region [46]. Thus, although the energy gained by the ions was determined theoretically, the current density carried by the beam ions remains a phenomenological parameter. The ion beam energy was calculated along the direction from the anode to the cathode. The calculation starts at the point where the electric force acting on the ion first exceeded the minimum ion drag force F from the plasma. At the point where the ion beam energy calculation start, the initial energy was assumed to be determined by the ion energy at this minimum and the ion temperature. Subsequently, the ions could increase their energy via acceleration in the electric fields E_z, which arise when magnetic flux leaks out onto the axis, i.e.,

$$\varepsilon_i = \varepsilon_0 + \int (eE_z - F)\,\mathrm{d}z\,,$$

where e is the electron charge. To accelerate the ions, the magnitude of the electric accelerating force along the axis must exceed the drag force, which can only occur if the electric fields are generated by anomalous resistivity arising in the plasma during its pinching on the chamber axis. When calculating the neutron yield using the beam–target mechanism, data on the DD reaction cross section from the ENDF/B-VII database [58] were used.

An upwind finite-difference scheme was used to approximate the differential equations of gas dynamics [59]. The electron and ion thermal conduction were calculated using explicit and implicit schemes. The implicit scheme employed an iterative line-sweep method over grid rows and columns [60]. To ensure the stability of the calculations, in both cases, an artificial limitation was imposed on the energy flux leaving a computational cell during each time step.

An implicit scheme with line sweeps was also used to calculate the distribution of magnetic and electric fields. In this approach, the calculation of the magnetic field components associated with the Alfvéen velocity was coupled with the calculation of the electric fields (see [46–48, 61]). This significantly relaxes the time-step restriction typical of explicit schemes due to the presence of low-density regions.

One of the issues in simulating plasma flows in Eulerian coordinates is how to perform calculations in regions where no matter remains (vacuum regions). Such regions arise behind the plasma sheath as it moves toward the chamber axis. To overcome this difficulty, it is necessary to assume that the density cannot be less than some minimum value ρ_{min}. At relatively large ρ_{min}, the gas density behind the plasma sheath is sufficiently high, resulting in current shunting in the region behind the sheath, and the process of plasma focusing on the axis is less pronounced. At small ρ_{min}, the computational time step begins to decrease due to the requirement for calculation stability. We studied the effect of the minimum value of the residual gas density in the vacuum region [47] and showed that satisfactory agreement with experiment is achieved at residual gas densities of $\leqslant 10^{-5}$ of the initial density.

Our simulations also showed that, the plasma in the 'vacuum' region behind the CPS experiences strong heating (apparently due to nonphysical counting effects). This heating is so strong that, despite the low density of the residual gas, it leads to a thermal pressure comparable to the magnetic pressure, partially shielding the pinch region from the current flowing through this low-density plasma. As a result, the pinch does not receive enough current, and conditions for neutron generation via the beam–target mechanism are not achieved. Increasing the voltage on the chamber axis, and consequently the neutron yield, was achieved in the calculation by limiting the ion and electron temperatures to 1 keV in the low-density region: where the density is 10 times or more lower than the initial density of the unperturbed gas. The lower temperature in the vacuum region contributed to greater plasma compression at the moment of focusing, since the region with the lower temperature (and pressure) provided less effective shielding of the magnetic field. After introducing a limit on the plasma temperature in the low-density region, it was possible to significantly improve the agreement between the experimental and calculated neutron yield.

3.1.1 Spherical plasma focus chambers. The MHD simulation of the plasma focus was performed taking into account the electrical circuit equations to the discharge current. The circuit current was determined by solving the electrical equation:

$$L\,\frac{\mathrm{d}I}{\mathrm{d}t} = U(t) - RI(t) - U_{PF}(t)\,, \qquad (11)$$

where L is the circuit inductance; $U(t) = U_0 - 1/C\int_0^t I(t)\,\mathrm{d}t$, U_0 is the battery charge voltage; C is the battery capacitance; R is the circuit resistance; and U_{PF} is the voltage at the chamber inlet, which was determined from the MHD simulations.

The calculations were performed for spherical plasma chambers with diameters of 120 and 340 mm. The geometry of a chamber with an anode diameter of 60 mm and a cathode diameter of 120 mm is shown in Fig. 6.

The initial conditions for the chamber calculations are summarized in the table. The chamber with a diameter of 120 mm was filled with a deuterium–tritium mixture, while the chamber with a diameter of 340 mm was filled with deuterium. The initial gas density was $\rho_0 = 4.8\times 10^{-6}$ g cm^{-3} (18 Torr) for the 120 mm diameter chamber and $\rho_0 = 2.6\times 10^{-6}$ g cm^{-3} (12 Torr) for the 340 mm diameter chamber. The initial temperatures of the ions and electrons were assumed to be $T_e = T_i = 11600$ K (1 eV). The boundary value of the magnetic field B_0 was specified in the cells adjacent to the insulator. To calculate B_0, the current in the circuit was found from Eqn (11). When calculating the

Chamber diameter	120 mm	340 mm
C, μF	70	400
L, nH	27	32
R, mΩ	3	1.5
U_0, kV	15–29	15–35
W_0, kJ	8–29	45–245
P_0, Torr	4–30	18–30
T_{e0}, eV	1	1
T_{i0}, eV	1	1

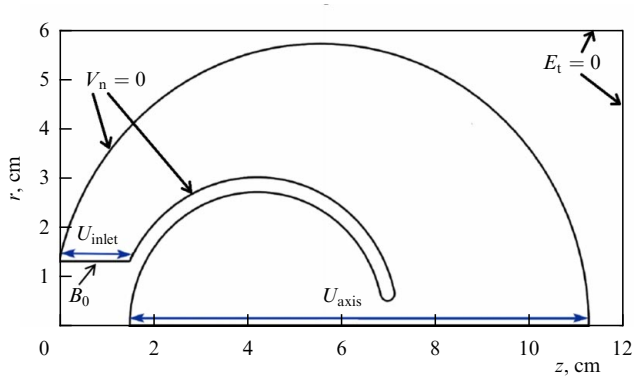

Figure 6. Geometry of the SFK chamber used in simulations (U_{inlet} is the voltage at the chamber inlet, U_{axis} is the voltage on the chamber axis) [47].

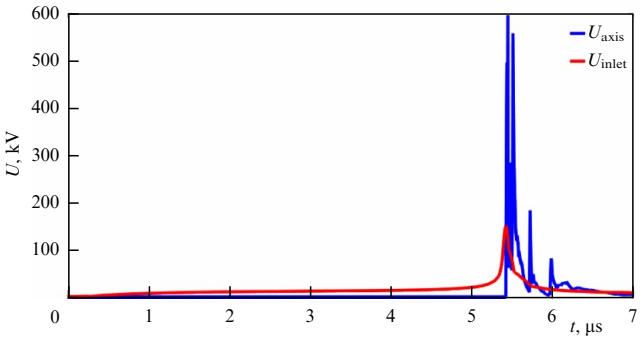

Figure 7. Voltage as a function of time for a chamber with a diameter of 340 mm, $U_0 = 30$ kV, $P_0 = 21$ Torr, D_2 gas [47].

boundary conditions, the normal component of the velocity and the tangential component of the electric field E_t at the boundary with the electrodes were assumed to be zero.

Figure 7 shows the voltages at the chamber inlet (U_{inlet}) and at the chamber axis (U_{axis}) obtained in the MHD calculation including the anomalous resistivity, for a spherical chamber with a cathode diameter of 340 mm and anode diameter of 180 mm, corresponding to the KPU-200 facility [62]. The charging voltage of the capacitor bank in the calculation was 30 kV. The voltage peak at the chamber inlet occurs at the moment of plasma sheath collapse and plasma focus formation. The peak voltage on the axis corresponds to the moment of pinch collapse and magnetic flux penetration to the chamber axis. The FWHM duration of the peak voltage at the chamber inlet is approximately 130 ns, and the voltage on the chamber axis has two peaks with FWHM durations of 20 and 15 ns. The axial voltage amplitude reaches 600 kV, which is approximately four times greater than the inlet voltage amplitude (150 kV). Moreover, the inlet voltage is five times greater than the capacitor bank voltage. Such a strong voltage amplification can lead to the generation of high-energy ions. During voltage peaks in the plasma focus, ions are accelerated along the chamber axis, generating beam–target neutrons. The maximum axial voltage corresponds to the maximum intensity of beam–target neutron generation. It should be noted that recent experiments [19, 20, 45, 63, 64] have observed ions accelerated to energies of several to tens of MeV at various facilities. These energies are tens (and even hundred) times higher than the energies that can be generated by the initial voltages on the current generators used in the experiments. Perhaps the electric field strengths obtained in our calculations, which, taking into account their dependence on coordinates and time, can accelerate ions to high energies, will help understand the mechanism by which such energetic ions are generated.

Figure 8 shows distributions of plasma density (Fig. 8a) and ion (Fig. 8b) and electron (Fig. 8c) temperature, obtained in MHD simulations for a chamber with a diameter of 340 mm. Figure 8a clearly shows that, as the CPS propagates, part of the gas mass is pressed toward the cathode. Note that the shape and position of the plasma sheath obtained in MHD simulations correlate well with experimental optical images of the CPS obtained in a number of studies. The time $t = 5.42$ μs shown in Fig. 8 corresponds to the peak voltage at the chamber inlet and the minimum pinch radius. At this moment, the plasma density in the pinch region reaches its maximum value. The time $t = 5.43$ μs corresponds to the peak voltage at the chamber axis (see Fig. 7) and the maximum neutron generation intensity. At this moment, the narrow pinch neck destroys, and the pinch begins to decay.

For comparison of the calculation results with the experimental data on the current, current derivative, and voltage in the chamber, Fig. 9 shows the experimental and calculated curves of current, voltage, and current derivative for PF facilities with chamber diameters of 120 mm (Figs 9a and 9b) and 340 mm (Fig. 9c). Note that to ensure agreement between the simulated and experimental time of the singularity occurrence and, accordingly, the focusing time of the plasma sheath, the initial density in a 340 mm diameter chamber is assumed to be 1.75 times lower than the real one. The reason for the difference between the calculated and experimental focusing times is apparently explained by the fact that in the experiment, due to the asymmetry of the CPS in the azimuthal direction, a filamentary (fibrous) structure of the sheath arises, and some of the gas leaks between the filaments and is not involved in the process of sweeping the plasma to the axis. It is not possible to fully take into account such effects in two-dimensional calculations; therefore, the simulations were carried out with a reduced value of the initial gas pressure [65, 66]. We can also mention some effects that could potentially lead to a faster arrival of the CPS to the axis. This is, for example, the detachment of the plasma from the anode, caused by the introduction of magnetic flux to the anode due to the Hall effect [67–69] (see also [30]). However, our attempts to take this effect into account in simulations by significantly reducing the initial gas density in the near-anode region on scales of $\sim c/\omega_{pi}$ (ω_{pi} is the plasma ion frequency) [30, 65], as well as attempts to take this effect into account in the MAGO chamber [30], which even include direct consideration of the Hall effect, did not lead to any noticeable decrease in the time of CPS arrival to the axis. The reasons for this are apparently the smallness of the scale $\sim c/\omega_{pi}$ compared to the characteristic scales of the problem, two-dimensional hydrodynamic mixing of this zone with large scales and relatively low temperatures, and, consequently, high collisionality of the plasma. It is also worth mentioning the erosion (washout) of the near-electrode material from the anode, which plays an important role in the MAGO chamber [30], but has not been studied for the plasma focus, and this effect can also suppress the detachment of plasma from the anode in experiments. A possible effect leading to the release of part of the plasma mass during the CPS acceleration and

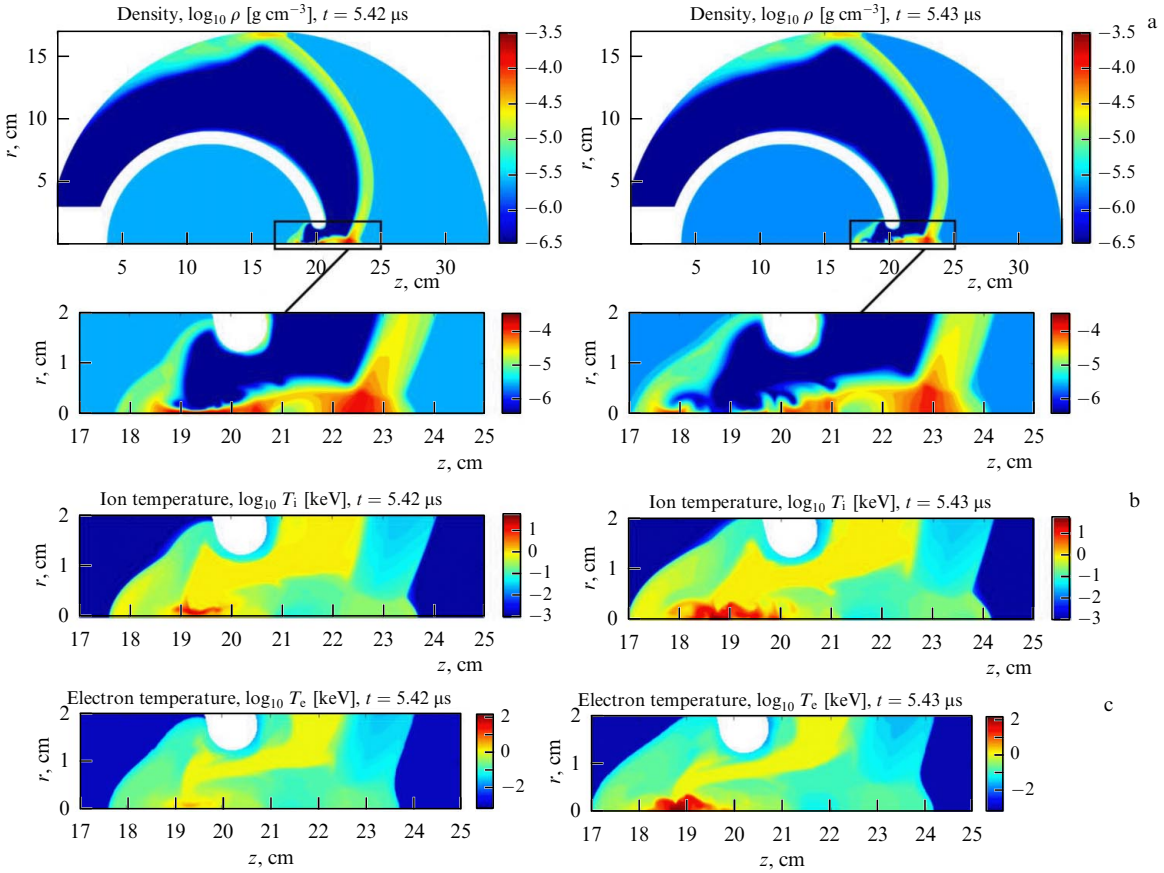

Figure 8. (a) Density distribution, $\log_{10}\rho$ [g cm^{-3}]; (b) ion temperature distribution, $\log_{10} T_i$ [keV]; and (c) electron temperature distribution, $\log_{10} T_e$ [keV] [47].

propagation toward the axis could be the Rayleigh–Taylor (RT) instability, the development of which at short wavelengths can lead to a release of part of the plasma mass, and, accordingly, to an additional acceleration of the remaining mass, as it occurs during the acceleration of liners [70]. However, for axisymmetric perturbations, this effect is quite well modeled [70] in two-dimensional MHD simulations. As for nonaxisymmetric perturbations, it is quite possible that their development leads to the fact that part of the plasma mass remains uninvolved in the propagation and forces a decrease in the plasma mass in two-dimensional simulations.

For the operating parameters of the PF facility given in Fig. 9a, the experimental neutron yield was $(3.0 \pm 0.6) \times 10^9$ DD neutrons. The calculated yield was 2.8×10^9 neutrons. For a 340 mm diameter chamber with the capacitor bank charged to 30 kV, the neutron yield was $(6.2 \pm 0.9) \times 10^{11}$ DD neutrons. The calculated neutron yield was 2.0×10^{11} neutrons, i.e., lower by a factor of 3.1 than the experimental yield.

The underestimation of the neutron yield calculation for a 340 mm diameter chamber occurred across the entire energy range for which the simulation was performed and reliable experimental neutron yield data were available. The discrepancy between the calculated and experimental yields can be partially explained by the presence of neutron emission anisotropy for the DD reaction. When measuring the neutron yield, the detectors were positioned close to the discharge chamber axis, and no correction for anisotropy was applied when determining the integral yield. However, according to the data presented in [71], the difference between the differential forward neutron yield cross section and the average yield over the solid angle can range from 1.9 to 3.5 for incident deuteron energies of 150–1000 keV. Assuming that the incident deuteron energy in our experiments was $\sim$ 150 keV, then one would expect the ratio of the experimental to calculated neutron yields to decrease from 3.1 to 1.6 when accounting for neutron yield anisotropy.

Our simulations also provided the neutron energy spectra in the 0°, 90° and 180° directions relative to the discharge chamber axis. These results were compared with experimental measurements of the DT neutron spectrum from the plasma focus in the same directions. Good agreement with the experiment was obtained for the position of the spectrum maximum for all three directions.

3.1.2 Gas-puff Z-pinches. In addition to the plasma focus, another possible configuration of a Z-pinch is a gas-puff Z-pinch. This type of research has been conducted on fast accelerators, starting with the experiments at the Angara-5-1 facility [12], where a significant neutron yield of 8×10^{11} DD neutrons per pulse was obtained at a current level of 2–2.5 MA with pulsed deuterium injection into the discharge gap. In the early 2000s, experiments were conducted at the Z facility [21–23], where a neutron yield of 4×10^{13} DD neutrons was obtained at a current level of 18 MA. The obtained data indicated a predominantly thermonuclear mechanism of neutron generation. Therefore, calculations of the fast Z-pinch operation [12], taking into account the pulsed gas puffing and using a two-dimensional MHD model that

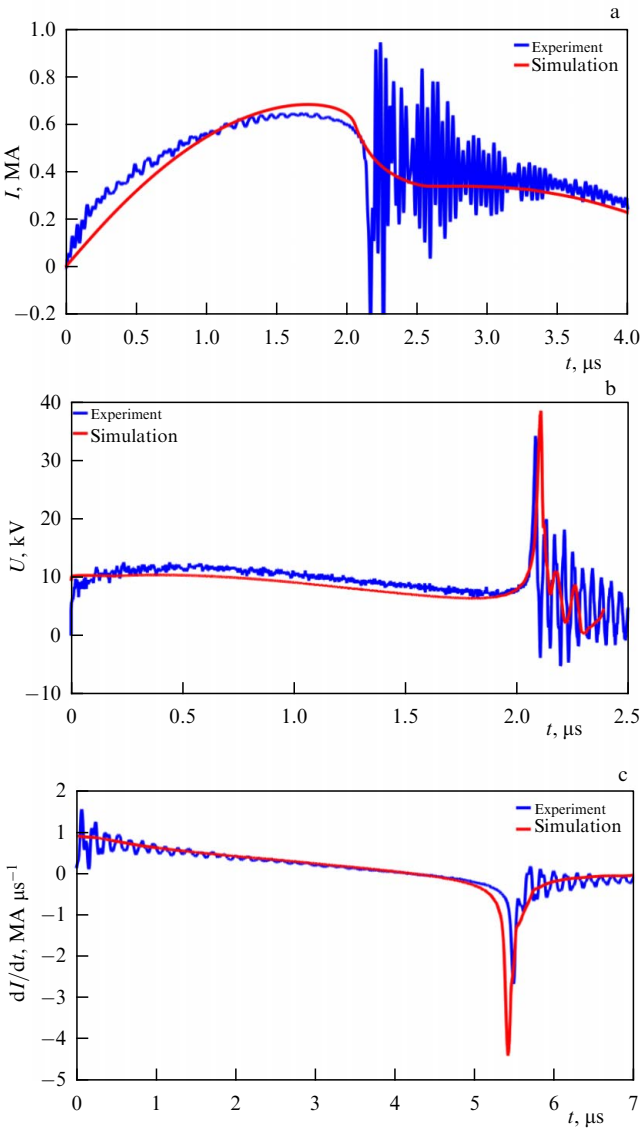

Figure 9. Comparison of simulations with experimental data: (a) current as a function of time for a chamber with a diameter of 120 mm, $U_0 = 19$ kV, $P_0 = 18$ Torr, and D_2 gas; (b) voltage as a function of time for a chamber with a diameter of 120 mm, $U_0 = 21$ kV, $P_0 = 18$ Torr, and DT gas; (c) current derivative as a function of time for a chamber with a diameter of 340 mm, $U_0 = 30$ kV, $P_0 = 12$ Torr, and D_2 gas [47].

includes the thermonuclear and beam–target neutron generation, are of interest. Such calculations were carried out in [72].

Figure 10 shows a rectangular computational domain (in z and r coordinates).

The region highlighted in white in Fig. 10 simulates the internal vacuum region of the Angara-5-1 load node [12]. Segment A corresponds to the anode, and C corresponds to the cathode. Region N denotes the nozzle used for deuterium injection into the discharge gap. At the initial moment in the calculations, the region was filled with rarefied deuterium with a molar mass of 4 g mol^{-1} and a background 'vacuum' density of $\sim 10^{-11}$ g cm^{-3}; the initial gas temperature was $T_0 = 0.0259$ eV. The region highlighted in Fig. 10 in gray represents the cathode material.

The boundaries of the computational domain ($z = 0$, $z = 10.2$, $r = 6$) were assumed to be cold, perfectly conducting walls with zero normal velocity, everywhere except for the

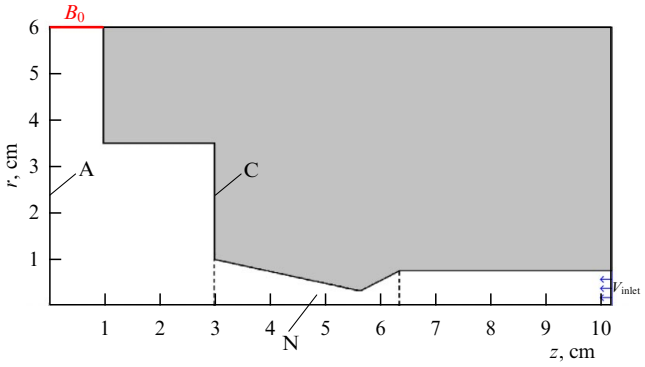

Figure 10. Calculated geometry of the Angara-5-1 load node: A — anode; C — cathode; N — nozzle (B_0 is the magnetic field at the boundary, and V_{inlet} is the deuterium inlet velocity [72]).

segment $z = 10.2, 0 \leqslant r \leqslant 0.76$ (highlighted in blue in Fig. 10), where the 'inlet velocity' boundary condition was specified to produce a gas mass flow after the high-speed valve was actuated [12]. On the segment $r = 6$, $0 \leqslant z \leqslant 1$ (highlighted in red in Fig. 10), the boundary magnetic field $B_0(t)$ was specified and determined from the current $I(t)$ given in [12]; $r = 0$ is the symmetry axis.

The calculations were performed in two stages. At the first (gas-dynamic) stage, the filling of the internal region of the load unit with molecular deuterium (D_2) with an initial temperature of $T_0 = 0.0259$ eV, through a high-speed valve and a supersonic nozzle, was simulated. The deuterium velocity at the inlet was $V_{\text{inlet}} = -10^5$ cm s^{-1} in accordance with estimates [12], the density at the inlet $\rho_{\text{inlet}} = 3 \times 10^{-4}$ g cm^{-3} was selected so as to ensure that the linear particle number density at the nozzle exit was 2×10^{18} cm^{-1} in ~ 30 μs, and that the density difference from the cathode to the anode was approximately an order of magnitude [12]. The calculations at the first stage were carried out in a single-temperature approximation; the magnetic and electric field distributions, conductivity, Joule heating, and radiation losses were not taken into account.

In the second stage, MHD calculations were performed to simulate plasma dynamics under the action of the current generated by the Angara-5-1 current pulse generator. When switching from the gas-dynamic to the MHD calculations, the initial data was reinitialized. The gas density and velocity distribution obtained in the first stage of the calculation was used as the initial data for the MHD calculations. The initial gas temperature was assumed to be $T_{i0} = T_{e0} = 0.5$ eV. The remaining parameters were calculated in accordance with the formulas used in the MHD calculations for an atomic mass of deuterium (2 g mol^{-1}).

Figure 11 shows the deuterium density distribution at various times on a computational grid with a step of $h = 0.01$ cm, obtained during the gas-dynamic stage of the calculations.

One can see from Fig. 11 that deuterium reaches the narrow section of the nozzle by 5 μs, forming a jet that reaches the anode and begins to propagate radially from the axis along the anode, with a reflected shock wave being formed. Overall, Fig. 11 shows that the filling of the internal region of the load node with deuterium is significantly nonuniform. At the time of the transition to the MHD calculation at 38.64 μs, the ratio of the density at the nozzle exit ($z = 3$ cm) to its minimum value near the anode is 9, which is consistent with experimental data [12].

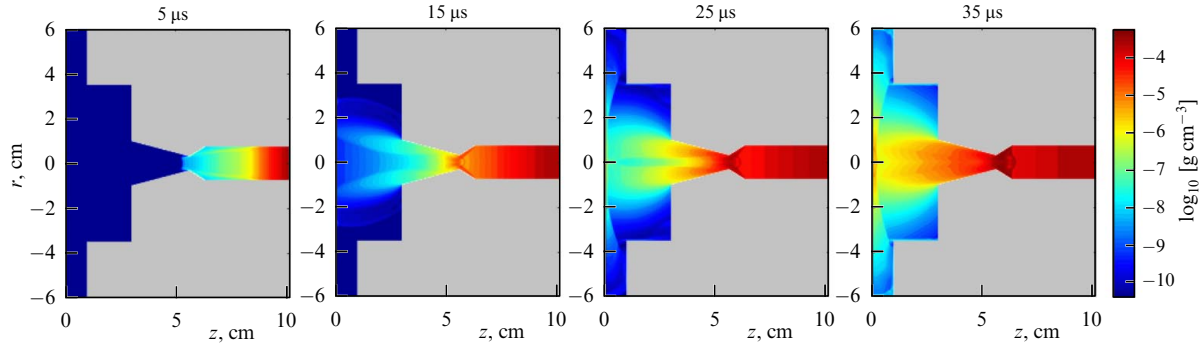

Figure 11. Deuterium density distribution at the gas-dynamic stage of the simulation at different times [72].

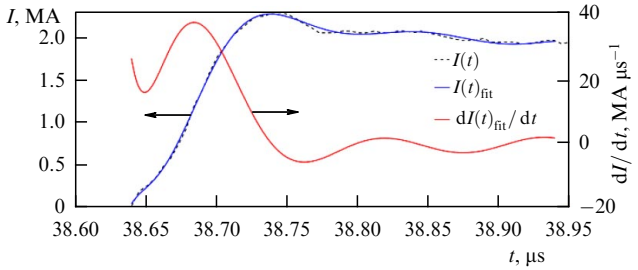

Figure 12. Current and current derivative of the Angara-5-1 generator as functions of time [72].

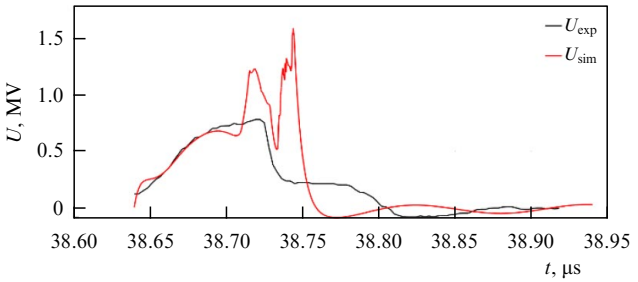

Figure 13. Experimental and simulated voltage as functions of time [73].

At the second stage of the calculation, plasma dynamics under the action of the current of the Angara-5-1 facility were simulated. Figure 12 shows the time dependence of the current $I(t)$ of the Angara-5-1 facility from [12] used in the MHD calculation, as well as its approximation by a 10th-degree polynomial $I_{\text{fit}}(t)$, and the current derivative $\mathrm{d}I_{\text{fit}}/\mathrm{d}t$, obtained by differentiating the approximating polynomial $I_{\text{fit}}(t)$ with respect to time. Figure 13 shows the experimental (U_{exp}) [12] and smoothed calculated (U_{calc}) time dependences of the generator voltage. One can see from Fig. 13 that it was not achieved full agreement between the experimental and calculated dependences. The rise in the calculated voltage curve at 38.64–38.65 μs is related to the behavior of the current derivative, which is caused by the inflection (bend) of $I(t)$ at 38.65 μs (see Fig. 12). An important difference between the calculated and experimental curves is that the calculated curve has a double voltage peak associated with pinching and the corresponding increase in inductance, which typically occurs in plasma focus Z-pinches. The experimental curve either lacks such a peak or shows a broader distribution, indicating that pinching occurs more slowly.

Figure 14 shows the plasma density distribution at various times before and after the pinch formation. At $t = 38.74$ μs, a plasma pinch forms on the axis. By $t = 38.742$ μs, it reaches a diameter of 0.2 cm and a density of 1.9×10^{-4} g cm^{-3}, which is approximately 18 times greater than the plasma density at the nozzle exit and 160 times greater than that near the anode at the moment of transition to the MHD simulations. The magnetic field at times of 38.742–38.744 μs, corresponding to the formation and decay of the pinch, reaches a value of $B \approx 4-6$ MG at a radius of 0.1–0.03 cm.

The calculations demonstrate significant heating of the vacuum regions behind the plasma sheath, with temperatures ranging from 0.05 to 1 keV. The ion temperature in the plasma sheath ranges from 3 to 5 keV, and at the moment of the pinch formation, it increases to ~ 20 keV. At the moment of the pinch destroy, the ion temperature in the resulting gap exceeds 1 MeV.

The calculated integrated neutron yield was 1.5×10^{11} DD neutrons per pulse, with the thermonuclear and beam–

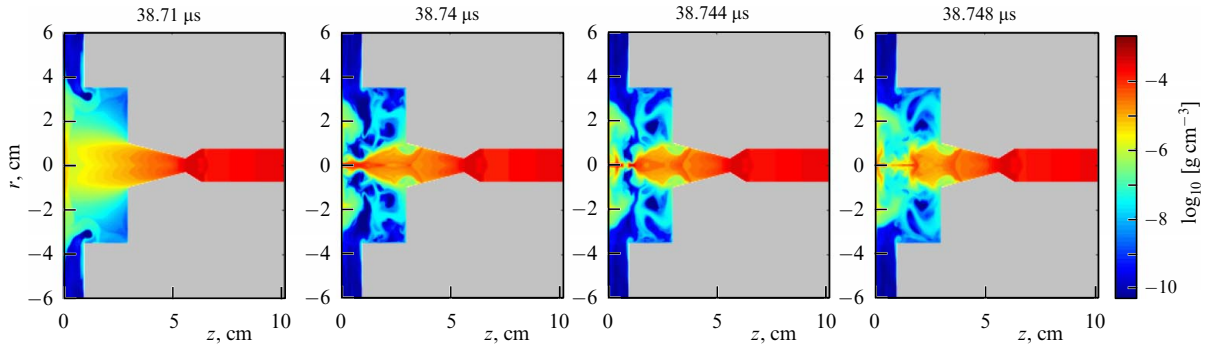

Figure 14. Plasma density distribution obtained in the MHD simulations at different times [72].

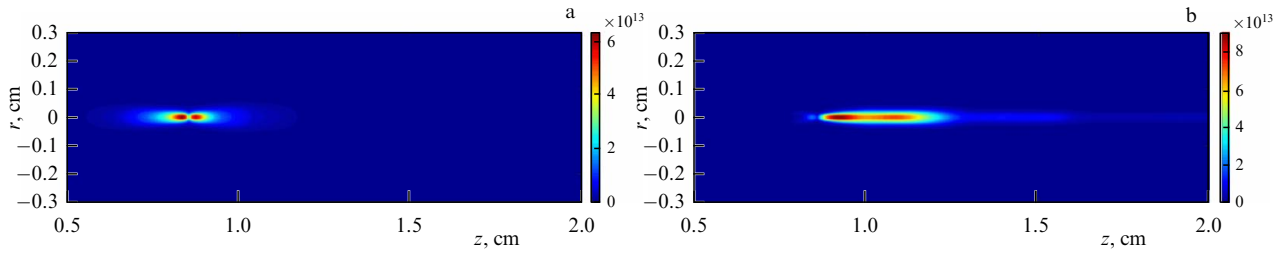

Figure 15. Distribution of the neutron yield of (a) thermonuclear neutrons and (b) beam–target neutrons per unit volume [72].

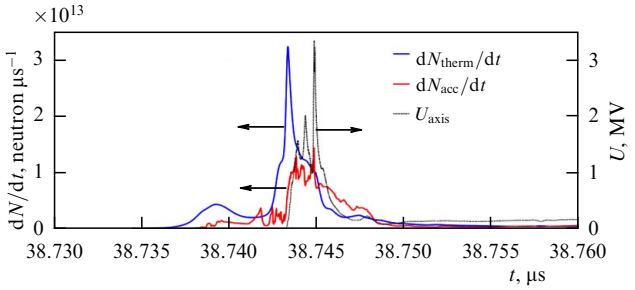

Figure 16. Neutron yield intensities for thermonuclear neutrons (dN_{therm}/dt) and accelerator neutrons (dN_{acc}/dt), and on-axis voltage (U_{axis}) as functions of time [72].

target components accounting for 9×10^{10} and 6×10^{10} DD neutrons, respectively. This ratio of thermonuclear and beam–target neutrons differs significantly from the results of neutron yield calculations in the plasma focus, where beam–target neutrons typically exceed thermonuclear neutrons by 2–3 orders of magnitude [46, 47].

Figure 15 shows the calculated distribution of thermonuclear and beam–target neutron yields per unit volume. Only the near-axis region, where neutron generation occurred, is shown. One can see from Fig. 15 that the length of the beam–target neutron generation region along the z axis is approximately three times greater than that of thermonuclear neutrons, amounting to ~ 0.2 cm. The radii of the generation region are similar, being ~ 0.3 cm for beam–target neutrons and ~ 0.2 cm for thermonuclear neutrons.

Figure 16 shows the neutron yield intensities for thermonuclear (dN_{therm}/dt) and beam–target neutrons (dN_{acc}/dt) and the on-axis voltage (U_{axis}) as functions of time. The graphs in Fig. 16 demonstrate that the positions of the dN_{acc}/dt and U_{axis} maxima are almost identical and correspond to the moment of pinch neck breakdown. The FWHM of the dN_{therm}/dt curve is 1 ns, while for dN_{acc}/dt it is 3 ns. The on-axis voltage reaches a maximum of 3.3 MV. The FWHM of the voltage pulse is 1.1–1.8 ns. The time interval of 38.744–38.748 μs, which contains the main voltage peak on the axis, corresponds to the neck destroy. Subsequent shorting of the current by the neck further leads to a noticeable decrease in the on-axis voltage.

In addition to the integral neutron yield, the calculation also demonstrates the distribution of the beam–target neutron yield with respect to the incident ion energy. It has a main peak in the energy range of 40–300 keV and a high-energy 'tail' of 300–1200 keV. Ninety percent of the neutron yield lies in the range of 55–900 keV. Estimates [12] place this energy range at 200–500 keV.

The neutron yield in the experiments [12] varied between 5×10^{10} to 8×10^{11} DD neutrons per pulse, depending on the delay between the signal from the nozzle gas pressure sensor and the moment the generator is started. In calculations with varying deuterium density and the time of transition to the MHD calculation, the yield ranged from 5×10^{10} to 1.5×10^{11} DD neutrons per pulse. In the calculations, it was not reproduced the experimental neutron yield of 8×10^{11} DD neutrons [12], which may indicate the need to adjust the beam–target mechanism model [46, 47] as applied to calculations of systems with pulsed gas injection.

3.2 Kinetic simulation

A kinetic description of charged particle motion in the particle-in-cell approximation in the CPS focusing region, coupled with the MHD approach for the rest of the plasma focus region, has been presented in a number of studies [36–38, 74, 75]. This task is very challenging, since a description of both ion and electron kinetics is required to describe kinetic instabilities and beam formation. Strictly speaking, this requires ensuring not only temporal resolution at the electron cyclotron frequency but also spatial resolution on the order of the electron Larmor radius (even without resolving the Debye length and assuming the plasma to be quasi-neutral). These conditions are difficult to achieve in practical simulations and are not always met. Nevertheless, even under these conditions, many interesting results have been obtained.

For example, qualitative agreement with experimental data on neutron yield at the plasma focus was obtained in [36, 38, 73]. Figure 17 shows a comparison of the calculated and measured neutron production rates dN/dt [38].

In [74], agreement with the experiment was achieved for the ion distribution in beams formed at the plasma focus (Fig. 18). Studies [74, 75] confirmed that the anomalous plasma resistivity can be caused by lower-hybrid drift instability, as assumed in phenomenological MHD simulations.

In [37], kinetic simulations were used to explain the observed decrease in neutron yield relative to the I^4 scaling law at currents above 3 MA in Z-pinch experiments. According to calculations [37] performed in a two-dimensional formulation for plasma with density perturbations serving as seeds for the RT instability (as well as the sausage instability) the following behavior was observed: at low currents ($I < 3$ MA), the neutron yield increases due to beam–target neutrons generated from collisions with high-energy ions that are accelerated to high energies in the electric fields arising from the development of instabilities (including both MHD and possibly kinetic instabilities). At the same time, at currents $I > 3$ MA, a decrease in the yield relative to the I^4 scaling is observed due to a reduction in plasma temperature in the pinch and an increase in the drag force

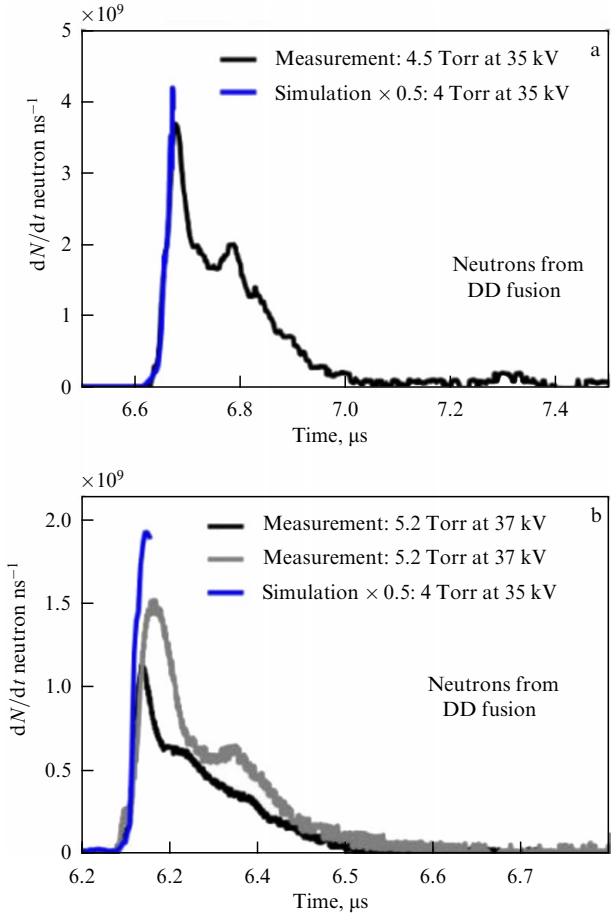

Figure 17. Simulated and measured neutron production rates dN/dt [38].

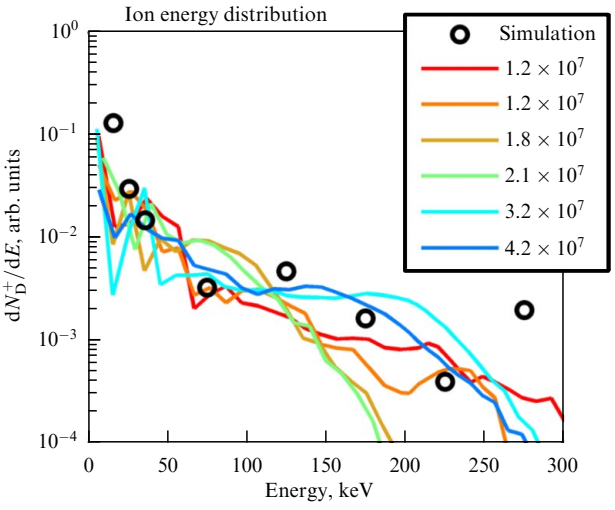

Figure 18. Simulated (black circles) and measured ion energy distributions [74].

acting on fast ions generated during the development of these instabilities. These ions, due to their short mean free paths, can no longer penetrate the dense pinch plasma and cannot gain additional energy from the electric field, resulting in a decrease in the beam–target neutron yield. Figure 19 shows the calculated neutron yields normalized to the I^4 scaling law, compared with the experimental data.

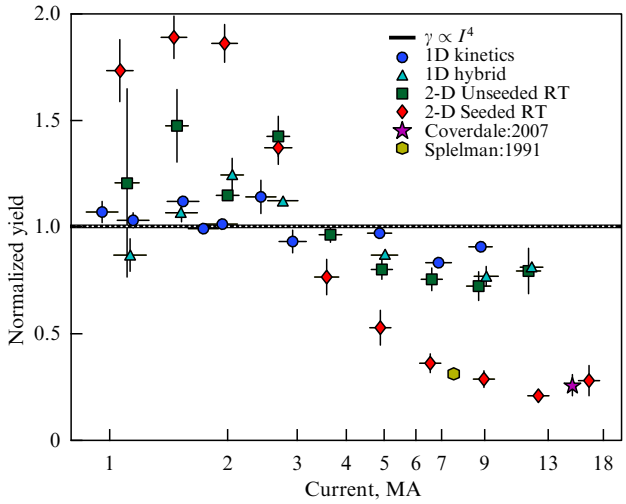

Figure 19. Neutron yield normalized to the I^4 scaling law, obtained in 1D and 2D simulations [37], compared with experimental data.

4. Conclusions

Simulation of the neck development showed that, due to the development of turbulence, a small-radius neck does not form and plasma does not flow out from the compression zone. Pressures, densities, and magnetic fields in the compression region do not increase indefinitely during compression but stabilize. High voltages are also not generated near the axis, which could facilitate ion beam formation and neutron generation via the beam–target mechanism. The calculations establish an MHD equilibrium state at the margin of the Kadomtsev instability. Therefore, to describe neutron generation in the beam–target mechanisms, it is necessary to take into account the kinetic processes responsible for high-voltage formation in the plasma.

Comparison of plasma dynamics calculations in spherical plasma focus chambers with experimental data demonstrated the adequacy of the MHD model and its applicability for studying the CPS dynamics in plasma focus chambers. Neutron yield calculations based on the beam–target mechanism model showed agreement with experimental results.

Plasma dynamics simulations for the Angara-5-1 facility provided a satisfactory description of the available experimental data on the gas density distribution in the discharge gap, the voltage at the load input, and the neutron yield. The following pinch parameters were obtained: diameter ~ 0.2 cm, density compression greater than 160, pinch temperature ~ 20 keV, and magnetic field at the pinch radius ~ 4–6 MG. The characteristic dimensions of the neutron generation region ($z \times r$) are $\sim 0.7 \times 0.03$ cm for beam–target neutrons and $\sim 0.2 \times 0.02$ cm for thermonuclear neutrons. The maximum neutron yield in the calculation was 1.5×10^{11} DD neutrons per pulse, with the thermonuclear and beam–target components of the neutron yield contributing for 9×10^{10} and 6×10^{10} DD neutrons, respectively.

Two-dimensional kinetic calculations of the plasma focus, performed for the final phase of pinch formation, show agreement with experimental data on neutron yield and ion distribution in the resulting beams and confirm that the anomalous plasma resistivity may be caused by the lower-

hybrid instability, as assumed in the phenomenological MHD simulations describing neutron generation in Z-pinches and plasma focus.

5. Appendix. Marginally stable Kadomtsev profiles

We will construct profiles of characteristic quantities in an equilibrium Z-pinch at the margin $m = 0$ of the interchange instability, i.e., when the equilibrium condition

$$\frac{\mathrm{d}p}{\mathrm{d}r} = -\frac{B}{4\pi r}\frac{\mathrm{d}}{\mathrm{d}r}(rB) \tag{A.1}$$

is satisfied and the equality sign is used instead of the inequality in the stability condition (7)

$$\frac{\mathrm{d}\ln p}{\mathrm{d}\ln r} = -\frac{4\gamma}{2+\beta\gamma}\,. \tag{A.2}$$

We will also correct an error in the original paper by B.B. Kadomtsev [49].

The equilibrium condition (A.1) can be rewritten as

$$\frac{\mathrm{d}\ln p}{\mathrm{d}\ln r} = \frac{1}{1+\beta}\left(\frac{\mathrm{d}\ln\beta}{\mathrm{d}\ln r} - 2\right). \tag{A.3}$$

Then, using (A.2) and (A.3), we obtain

$$\frac{\mathrm{d}\ln\beta}{\mathrm{d}\ln r} = \frac{4 - 2\gamma\beta - 4\gamma}{2+\gamma\beta}\,. \tag{A.4}$$

Integrating (A.4), we obtain the dependence of the radius on β

$$r = a\,\frac{(\beta + 2 - (2/\gamma))^{(2-\gamma)/2(\gamma-1)}}{\beta^{1/(2(\gamma-1))}}\,, \tag{A.5}$$

where a is an integration constant. For $\gamma = 5/3$, Eqn (A.5) yields

$$r = a\,\frac{(\beta+0.8)^{1/4}}{\beta^{3/4}}\,. \tag{A.6}$$

To find the dependence of p on β, we eliminate the radius by dividing (A.3) by (A.4). Then, after simple transformations, we obtain

$$\frac{\mathrm{d}p}{p} = \frac{\gamma}{\gamma-1}\left(\frac{1}{\beta} + \frac{\gamma}{2-\gamma\beta-2\gamma}\right)\mathrm{d}\beta\,. \tag{A.7}$$

Integrating (A.7), we obtain the dependence of pressure on β:

$$p = p_0\left(\frac{\beta}{\beta+2-(2/\gamma)}\right)^{\gamma/(\gamma-1)}\,, \tag{A.8}$$

where p_0 is an integration constant. For $\gamma = 5/3$, Eqn (A.8) yields

$$p = p_0\left(\frac{\beta}{\beta+0.8}\right)^{5/2}\,, \tag{A.9}$$

where p_0 is the pressure at $r = 0$, i.e., as $\beta \to \infty$. Relations (A.5) and (A.8), or (A.6) and (A.9), define the dependence of pressure on radius in parametric form. The corresponding dependences of pressure and magnetic field on radius are shown by solid curves for $\gamma = 5/3$ (Fig. 20).

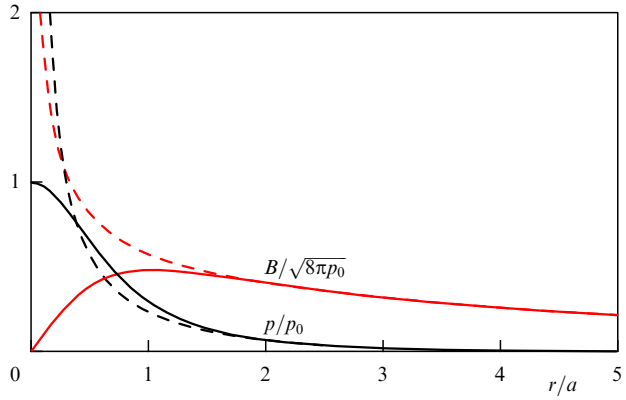

Figure 20. Pressure (p) and magnetic field (B) profiles (solid lines correspond to $m = 0$; dashed lines, to $m = 1$).

Let us now consider the equilibrium Z-pinch at the margin of the $m = 1$ instability. Using stability condition (8) and equilibrium condition (A.1), which can be written as

$$\frac{\mathrm{d}\ln p}{\mathrm{d}\ln r} = \frac{1}{1+\beta}\left(\frac{\mathrm{d}\ln\beta}{\mathrm{d}\ln r} - 2\right),$$

where $\beta = (8\pi p)/B^2$, we obtain $\beta = Cr + 1$, or

$$p = \frac{B^2}{8\pi}(Cr+1)\,, \tag{A.10}$$

where C is a constant.

Substituting (A.10) into equilibrium condition (A.1), we obtain

$$B = \frac{C_1}{\sqrt{r}}\,. \tag{A.11}$$

Next, substituting (A.11) into (A.10), we obtain

$$p = \frac{C_1^2}{8\pi r} + C_2\,, \tag{A.12}$$

where C_1 and C_2 are constants. Formulas (A.11) and (A.12) show that if the $m = 1$ instability leads to an effective rearrangement of the magnetic field toward the Z-pinch stability margin, then the effective magnetic field and pressure of the substance will accumulate near the axis according to the laws $1/\sqrt{r}$ and $1/r$, and β will tend to unity.

To construct a solution at the stability boundary for both $m = 0$ and $m = 1$, we match solutions (A.5), (A.8) and (A.11), (A.12) at the point where conditions (A.2) and (8) coincide, i.e., at $\beta_0 = 2/3\gamma$. By equating the pressure and magnetic field at this point, we relate the constants C_1, C_2 and a, p_0

$$C_1 = \sqrt{8\pi p_0 a\,\frac{B_0^{1/(2(\gamma-1))}}{(0.8+\beta_0)^{(3\gamma-2)/(2(\gamma-1))}}}\,,$$

$$\frac{C_1^2}{8\pi} = p_0 a\,\frac{\beta_0^{1/(2(\gamma-1))}}{(0.8+\beta_0)^{(3\gamma-2)/(2(\gamma-1))}}\,,$$

$$C_2 = -p_0\left(\frac{\beta_0}{0.8+\beta_0}\right)^{\gamma/(\gamma-1)}\left(\frac{1-\beta_0}{\beta_0}\right).$$

For $\gamma = 5/3$, the relationship between C_1, C_2 and the constants p_0 and a from (A.6) and (A.9) will have the form:

$$C_1 = \sqrt{8\pi p_0 a \, \frac{B_0^{3/4}}{(0.8+\beta_0)^{9/4}}},$$

$$\frac{C_1^2}{8\pi} = p_0 a \, \frac{\beta_0^{3/4}}{(0.8+\beta_0)^{9/4}},$$

$$C_2 = -p_0 \left(\frac{\beta_0}{0.8+\beta_0}\right)^{5/2} \left(\frac{1-\beta_0}{\beta_0}\right). \qquad \text{(A.13)}$$

Since in this case $\beta_0 = 2/5$, the constants in (A.13) are equal to

$$\frac{\beta_0^{3/4}}{(0.8+\beta_0)^{9/4}} \approx 0.334, \quad \left(\frac{\beta_0}{0.8+\beta_0}\right)^{5/2} \left(\frac{1-\beta_0}{\beta_0}\right) \approx 0.0962.$$

References

1. D'yachenko V F, Imshennik V S, in *Voprosy Teorii Plazmy* Iss. 8 (Ed. M A Leontovich) (Moscow: Atomizdat, 1974) p. 164; Translated into English: in *Reviews Plasma Physics* Vol. 8 (Ed. M A Leontovich) (Boston, MA: Consultants Bureau, 1980) p. 199, DOI:10.1007/978-1-4615-7814-7_3
2. Vikhrev V V, Braginskii S I, in *Voprosy Teorii Plazmy* Iss. 10 (Ed. M A Leontovich) (Moscow: Atomizdat, 1980) p. 243; in *Review Plasma Physics* Vol. 10 (Ed. M A Leontovich) (New York: Consultants Bureau, 1986) p. 425
3. Ryutov D D, Derzon M S, Matzen M K *Rev. Mod. Phys.* **72** 167 (2000)
4. Haines M G *Plasma Phys. Control. Fusion* **53** 093001 (2011)
5. Ise J, Pyle R V, in *Conf. on Controlled Thermonuclear Reactions, Princeton Univ., 17–20 October 1955, TID-7503* (Washington, DC: USAEC, 1955) p. 218
6. Artsimovich L A et al. *Atom. Energ.* **1** (3) 84 (1956); *Sov. J. Atom. Energy* **1** 375 (1956)
7. Gilbert F C et al., in *Conf. on Controlled Thermonuclear Reactions, Gaitlinburg, TN, 4–7 June 1956 TID-7520* Pt. 1 (Washington, DC: USAEC, 1956) p. 144; Dunaway R, in *Conf. on Controlled Thermonuclear Reactions, Gaitlinburg, TN, 4–7 June 1956 TID-7520* Pt. 1 (Washington, DC: USAEC, 1956) p. 127
8. Filippov N V, Filippova T I, Vinogradov V P *Nucl. Fusion Suppl.* **2** 577 (1962)
9. Mather J W *Phys. Fluids Suppl.* **7** 5 (1964)
10. Makeev N G, Rumyantsev V G, Maslov V V *Entsiklopediya Nizkotemperaturnoi Plazmy* (Encyclopedia of Low-Temperature Plasma) Ser. B, Vol. IX-3 (Ed. V A Gribkov) (Moscow: Yanus, 2007) p. 176
11. Makeev N G, Rumyantsev V G, Cheremukhin G N, in *Fizika i Tekhnika Impul'snykh Istochnikov Ioniziruyushchikh Izluchenii dlya Issledovaniya Bystroprotekayushchikh Protsessov* (Physics and Technology of Pulsed Sources of Ionizing Radiation for the Study of Fast Processes) (Ed. N G Makeev) (Sarov: RFYaTs–VNIIEF, 1996) p. 281
12. Batyunin A V et al. *Sov. J. Plasma Phys.* **16** 597 (1990); *Fiz. Plazmy* **16** 1027 (1990)
13. Klir D et al. *Plasma Phys. Control. Fusion* **52** 065013 (2010)
14. Lee S, Serban A *IEEE Trans. Plasma Sci.* **24** 1101 (1996)
15. Mikhailov Yu V, Lemeshko B D, Prokuratov I A *Plasma Phys. Rep.* **45** 334 (2019); *Fiz. Plazmy* **45** 323 (2019)
16. Gribkov V A et al. *J. Phys. D* **40** 3592 (2007)
17. Ablesimov V E et al. *Plasma Phys. Rep.* **36** 403 (2010); *Fiz. Plazmy* **36** 396 (2010)
18. Klir D et al. *Phys. Plasmas* **15** 032701 (2008)
19. Klir D et al. *New J. Phys.* **20** 053064 (2018)
20. Klir D et al. *Matter Radiat. Extremes* **5** 026401 (2020)
21. Velikovich A L et al. *Phys. Plasmas* **14** 022701 (2007)
22. Coverdale C A et al. *Phys. Plasmas* **14** 022706 (2007)
23. Coverdale C A et al. *Phys. Plasmas* **14** 056309 (2007)
24. Stanislawski J et al. *Nucleonika* **46** S73 (2001)
25. Milanese M M *Rev. Sci. Instrum.* **77** 036106 (2006)
26. Grabovskii E V et al. *Vopr. Atom. Nauki Tekh. Ser. Termoyad. Sintez* **45** (1) 119 (2022)
27. Trubnikov B A, Zhdanov S K *JETP Lett.* **41** 358 (1985); *Pis'ma Zh. Eksp. Teor. Fiz.* **41** (7) 292 (1985)
28. Zhdanov S K, Trubnikov B A *Sov. Phys. JETP* **63** 809 (1986); *Zh. Eksp. Teor. Fiz.* **90** 1380 (1986)
29. Garanin S F, Chernyshev Yu D *Fiz. Plazmy* **13** 974 (1987)
30. Garanin S F *Fizicheskie Protsessy v Sistemakh MAGO-MTF* (Sarov: RFYaTs–VNIIEF, 2012); Translated into English: "Physical Processes in the MAGO/MTF Systems," LA-UR-13-29094 (Los Alamos, 2013)
31. Vikhrev V V *Sov. J. Plasma Phys.* **12** 735 (1986); *Fiz. Plazmy* **12** 454 (1986)
32. Trubnikov B A *Sov. J. Plasma Phys.* **12** 271 (1986); *Fiz. Plazmy* **12** 468 (1986)
33. Yan'kov V V *Sov. J. Plasma Phys.* **17** 305 (1991); *Fiz. Plazmy* **17** 521 (1991)
34. Shan B, Lee P, Lee S *Sing. J. Phys.* **16** 25 (2000)
35. Lee S *J. Fusion Energy* **33** 319 (2014)
36. Schmidt A et al. *Phys. Plasmas* **21** 102703 (2014)
37. Offermann D T et al. *Phys. Rev. Lett.* **116** 195001 (2016)
38. Bennett N et al. *Phys. Plasmas* **24** 012702 (2017)
39. Landau L D, Lifshitz E M *Elektrodinamika Sploshnykh Sred* (Moscow: Nauka, 1982); Translated into English: *Electrodynamics of Continuous Media* (New York: Pergamon Press, 1984)
40. Trubnikov B A, in *Fizika Plazmy i Problema Upravlyaemykh Termoyadernykh Reaktsii* (Plasma Physics and the Problem of Controlled Thermonuclear Reactions) Vol. 1 (Exec. Ed. M A Leontovich) (Moscow: Izd. AN SSSR, 1958) p. 289
41. Kruskal M, Schwarzschild M *Proc. R. Soc. London A* **223** 348 (1954) DOI:10.1098/rspa.1954.0120
42. Shafranov V D *Sov. J. Atom. Energy* **1** 709 (1956); *Atom. Energ.* **1** (5) 38 (1956)
43. Book D L, Ott E, Lampe M *Phys. Fluids* **19** 1982 (1976)
44. Yan'kov V V, Preprint IAE-4218/7 (Moscow: I.V. Kurchatov Institute of Atomic Energy, 1985)
45. Lebedev S V, Frank A, Ryutov D D *Rev. Mod. Phys.* **91** 025002 (2019)
46. Garanin S F, Mamyshev V I *Plasma Phys. Rep.* **34** 639 (2008); *Fiz. Plazmy* **34** 695 (2008)
47. Garanin S F et al. *Plasma Phys. Rep.* **46** 978 (2020); *Fiz. Plazmy* **46** 890 (2020)
48. Garanin S F, Dolinskii V Yu *Plasma Phys. Rep.* **47** 814 (2021); *Fiz. Plazmy* **47** 728 (2021)
49. Kadomtsev B B, in *Voprosy Teorii Plazmy* Iss. 2 (Ed. M A Leontovich) (Moscow: Atomizdat, 1962) p. 132; Translated into English: in *Reviews of Plasma Physics* Vol. 2 (Ed. M A Leontovich) (New York: Consultants Bureau, 1966) p. 153
50. Braginskii S I, in *Voprosy Teorii Plazmy* Iss. 1 (Ed. M A Leontovich) (Moscow: Atomizdat, 1963) p. 18; Translated into English: in *Reviews in Plasma Physics* Vol. 1 (Ed. M A Leontovich) (New York: Consultants Bureau, 1965) p. 205
51. Lifshitz E M, Pitaevskii L P *Fizicheskaya Kinetika* (Moscow: Nauka, 1979); Translated into English: *Physical Kinetics* (Oxford: Pergamon Press, 1981)
52. Davidson R C, Gladd N T *Phys. Fluids* **18** 1327 (1975)
53. Krall N A, Liewer P C *Phys. Rev. A* **4** 2094 (1971)
54. Goedbloed J P, Pyatak A I, Sizonenko V L *Sov. Phys. JETP* **37** 1051 (1973); *Zh. Eksp. Teor. Fiz.* **64** 2084 (1973)
55. Sasorov P V *Sov. J. Plasma Phys.* **18** 143 (1992); *Fiz. Plazmy* **18** 275 (1992)
56. Kadomtsev B B *Kollektivnye Yavleniya v Plazme* (Cooperative Effects in Plasmas) (Moscow: Nauka, 1976); Translated into English: in *Reviews of Plasma Physics* Vol. 22 (Ed. V D Shafranov) (New York: Kluwer Acad. Plenum Publ., 2001) p. 1, DOI:10.1007/978-1-4615-1309-4_1
57. Trubnikov B A *Teoriya Plazmy* (Theory of Plasmas) (Moscow: Energoatomizdat, 1996)
58. Chadwick M B et al. *Nucl. Data Sheets* **107** 2931 (2006)
59. Fletcher C A J *Vychislitel'nye Metody v Dinamike Zhidkostei* Vol. 1 *Osnovnye Polozheniya i Obshchie Metody* (Moscow: Mir, 1991);

Translated from English: *Computational Techniques for Fluid Dynamics* Vol. 1 *Fundamental and General Techniques* (Berlin: Springer, 1988) DOI:10.1007/ 978-3-642-97035-1
60. Samarskii A A, Popov Yu P *Raznostnye Metody Resheniya Zadach Gazovoi Dinamiki* (Difference Methods for Solving Gas Dynamics Problems) (Moscow: Nauka, 1992)
61. Gaganov V V, Garanin S F, Dolinskii V Yu *Plasma Phys. Rep.* **49** 428 (2023); *Fiz. Plazmy* **49** 332 (2023)
62. Zavyalov N V et al. *Plasma Phys. Rep.* **39** 243 (2013); *Fiz. Plazmy* **39** 276 (2013)
63. Sohrabi M, Zarinshad A, Habibi M *Sci. Rep.* **6** 38843 (2016)
64. Ito H, Nishino Y, Masugata K *J. Korean Phys. Soc.* **59** 3674 (2011)
65. Dolinskii V Yu et al., in *Proc. of the 16th Intern. Conf. on Megagauss Magnetic Field Generation and Related Topics, Kashiwa, 2018*, p. 131
66. Garanin S F et al., in *XLVI Mezhdunarodnaya Zvenigorodskaya Konf. po Fizike Plazmy i Upravlyaemomy Termoyadernomy Sintezu, ICAF-2019, 18–22 Marta 2019, g. Zvenigorod* (XLVI Intern. Zvenogorod Conf. on Plasma Physics and Controlled Fusion, ICAF-2019, March 18–22, 2019, Zvenigorod) (Moscow: PLAZ-MAIOFAN, 2019) p. 122
67. Sasorov P V *Fiz. Plazmy* **16** 1236 (1990)
68. Garanin S F, Mamyshev V I *Fiz. Plazmy* **16** 1218 (1990)
69. Ananyev S S, Suslin S V *Fusion Eng. Design* **137** 338 (2018)
70. Garanin S F, Buyko A M, Yakubov V B *J. Appl. Mech. Tech. Phys.* **58** 779 (2017) DOI:10.1134/S0021894417050030; *Prikl. Mekh. Tekh. Fiz.* **58** (5) 26 (2017)
71. Liskien H, Paulsen A *Atom. Data Nucl. Data Tables* **11** 569 (1973)
72. Garanin S F, Dolinskii V Yu *Plasma Phys. Rep.* **50** 948 (2024); *Fiz. Plazmy* **50** 887 (2024)
73. Schmidt A, Tang V, Welch D *Phys. Rev. Lett.* **109** 205003 (2012)
74. Schmidt A et al. *Phys. Rev. E* **89** 061101 (2014)